13th ewtec 2019
Proceedings of the 13th European Wave and Tidal Energy Conference 1-6 Sept 2019, Naples, Italy

Influence of floater geometry on snap loads in mooring systems for wave energy converters

Johannes Palm and Claes Eskilsson

***Abstract*—Mooring systems for floating wave energy converters often rely on floaters to allow for minimum restraints of the body motion in heavy. However, the inclusion of floaters also introduce possible slack-taut scenarios induced by the dynamic response of the floater in relation to the fair-lead point of the mooring. This can increase the occurrence of snap loads. The present study outlines the work to include floaters and sinks into a high-order discontinuous Galerkin model for mooring cable dynamics. Numerical simulations of a mooring leg adapted from the Waves4Power full-scale device are performed, and the results from varying the floater geometry are analysed. For this case the floater influence on the occurrence of snap loads was clearly evident. There is a strong correlation between floater pitch response and cable slack in the upper mooring cable. For a floater with constant buoyancy, increasing the floater height and thereby increasing the pitch inertia of the floater is shown to decrease the range of frequencies where cable slack occurs. It is illustrated that for some cases, changing floater geometry can avoid slack altogether. A careful design of the floater geometry can thus make a large difference for the dynamic load factor of the mooring system.**

***Index Terms*—Mooring cables, floaters, snap load, floating wave energy converters.**

I. Introduction

MOORING of wave energy converters (WECs) is an area that has received increased interest lately as more devices approach sea-trials in larger scales, and subsequently also harsher weather conditions. Especially concepts based on wave activated bodies (such as floating point absorbers) put special demands on the mooring design and functionality.

In contrast to most traditional fields of mooring where the floating body is to be kept as stationary as possible, the mooring system of a floating point absorber is to allow maximum motion in the energy extracting modes while restraining the motion in the remaining modes [1]. An often used way to achieve this for heaving devices is through the use of *floaters*. A floater is a mooring element which provides buoyancy to the system. The idea is to use the floater to divide the cable into an almost vertical lower cable leg and a near-horizontal top cable leg attached to the wave energy converter (WEC), so that mainly horizontal forces are applied to the WEC. An example of such a mooring solution is the Waves4Power [2] device deployed at Runde, Norway - see Fig. 1. The use of floaters and sinks can be expected to increase in the mooring systems of marine renewable devices if the approach of inter-moored or shared mooring of wave energy arrays becomes adopted [3], [4].

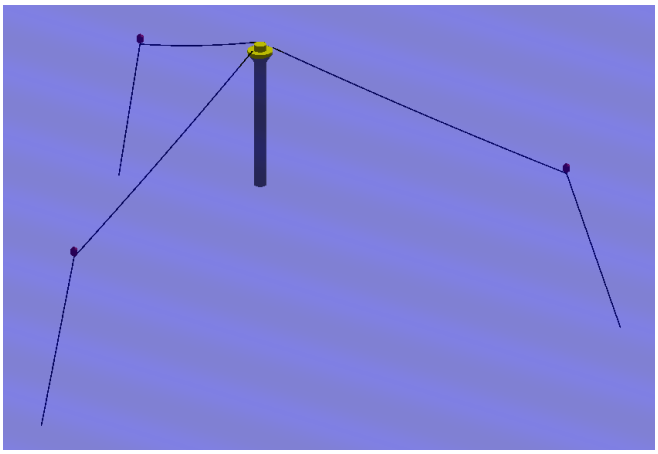

(a)

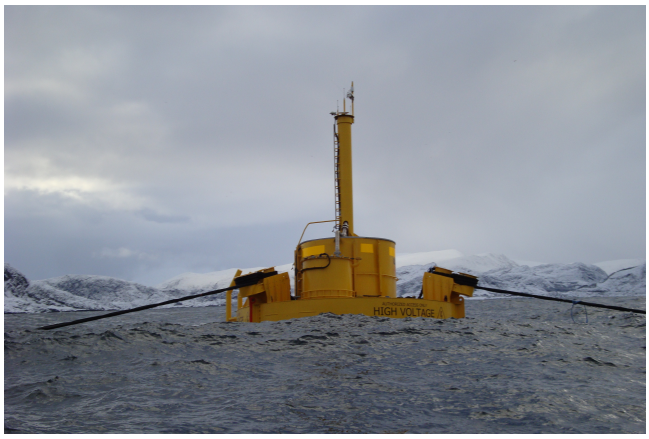

(b)

Fig. 1. Mooring system of the Waves4Power device. (a) Schematic layout showing the floaters and the WEC. (b) Photo from Runde full-scale sea-trial showing the top legs of the mooring cables. From [5]

Another area that mooring of wave energy converters can be expected to differ from the traditional marine industries is the occurrence of *snap loads* in the cables. A snap load typically occur when the mooring line is re-tightened after a period of slack. The load is essentially a discontinuous shock wave and the amplitude can be significantly higher than the underlying dynamic mooring loads. For traditional offshore structures mooring standards, e.g. DNV-OS-301 [6], state that mooring systems should be designed to avoid

Paper no: 1375. Part of track: Station-keeping, mooring and foundations. This work was supported by the Swedish Energy Agency under project number 42246-1.

J. Palm is with the Department of Mechanics and Maritime Sciences, Chalmers University of Technology, SE-412 96 Gothenburg, Sweden (e-mail: johannes.palm@chalmers.se).

C. Eskilsson is with the Department of Civil Engineering, Aalborg University, Thomas Manns Vej 23, DK-9220 Aalborg Ø, Denmark (e-mail: cge@civil.aau.dk).

snap loads. This seems difficult to realize for wave energy devices. The combination of large amplitude motion, small device displacement and limited water depth makes it hard to design the mooring system so that snap loads are always avoided.

A. Snap loads

As mentioned above, snap loads are tension shock waves that propagate along the cable [7]. The most common cause of a snap load is when a cable goes back into tension after a period of slack. The snap load amplitude is in this case dependent on the material stiffness and the local strain rate of the cable at the instant it returns to tension [8]. A second cause for snap load generation is when the touch-down point velocity of a chain exceeds the transverse wave speed of the cable [9], [10]. A third cause of snapping is due to nonlinear material stiffness, where a shock wave forms from a smooth initial condition [11].

Snap loads in mooring cables for marine renewable energy devices have been identified to cause damage to the mooring systems in both tank and field tests of WECs. Thies et al. [12] performed tank experiments of a WEC moored with fibre-ropes and floaters. The experiments showed the occurrence of snap loads and in a subsequent estimation of fatigue life, the snap loads were stated to significantly contribute to the fatigue damage. Experimental tests of the Uppsala WEC [13] showed snap loads in the taut steel-wire mooring. The snapping was generated by slack conditions caused by the translator moving down slower than the buoy (the Uppsala WEC has a bottom-mounted linear generator). The same behaviour was also identified in sea-trials [13]. Hann et al. [14] performed tank tests of a taut-moored WEC subjected to NewYear wave groups. It was shown that a series of consecutive snap loads were associated with the passing of the peak wave. Harnois [15] analyzed mooring data from a slack moored WEC deployed at the South West Mooring Test Facility, UK. Harnois identified possible snap events but highlights the difficulties involved in formally categorizing a peak mooring load as a snapping event.

B. Floaters

In this work we will consistently use the term floater to label a mooring element which: (i) has a net buoyancy when submerged; and (ii) can be regarded as a small rigid body for which the Morison equation of motion applies [16]. Additionally, a *sinker* can in this context be described as a floater with a negative buoyancy, i.e. a clump-weight on the mooring system. The use and effect of this type of mooring elements has been extensively studied in the literature for oil and gas applications, both experimentally and numerically, e.g. [17], [18]

Focusing on wave energy applications the mooring leg consisting of two segments with a floater has been utilized for e.g. the Pelamis attunator [19] and the Waves4Power point absorber [20]. Fitzgerald and Bergdahl [21] analysed the performance of a submerged buoy and a clump-weight for a moored WEC via static and dynamic simulations, concluding that the loads are significantly reduced from the simple catenary chain in slack-snap conditions. However, they also point out the weakness in sustaining a static side load, as the studied system was very compliant and had a low horizontal stiffness. Paredes et al. [22] compared the two floater-sinker mooring configurations with the catenary mooring chain. They showed similar performance overall but several differences between the response of the mooring types were highlighted. Vicente et al. [23] investigated the influence of floater location for a slack moored WEC. It was shown that a floater close to the surface and horisontally close to the anchor point yielded higher power absorption and smaller horizontal displacement of the WEC. Ortiz et al. [24] developed a surrogate model in order to optimize the mooring system for a heaving point absorber with regard to power production. The size of the floaters was one of the optimized parameters.

C. Paper contribution

Previous studies on mooring system with attached floaters have optimized the floater size and location with regard to maximising the power production [23], [24], but there has been less focus on the possibility of snapping events. The aim of the present paper is to focus on the slack-snap conditions of a typical WEC mooring systems with attached floaters. The study presents to some details the implementation of floaters and sinks in the the high-order discontinuous Galerkin mooring model Moody [25], [26]. In commercial mooring packages, floater elements are typically handled via lumped parameter Morison bodies, see e.g. [27]. In this work we implement the floater as a rigid body motion framework for submerged cylinders, where the rotational response is shown to have a large impact on the mooring response. The floater implementation is then utilized in order to evaluate the influence of floater geometry on the possibility of snapping events. By numerical simulations of a mooring leg with dimensions inspired by the Waves4Power mooring system utilized at the Runde trials, we perform a screening using harmonic motion of the fair-lead. The influence of floater size, amplitude and frequency of the fair-lead motion are investigated.

II. Governing equations

D. Cable dynamics

For a cable of length L, we use the unstretched cable coordinate $s \in [0, L]$ to express the global coordinate position vector of the cable as $\vec{r} = [r_1(s), r_2(s), r_3(s)]^{\mathrm{T}}$. Under the assumption of negligible bending stiffness, the equation of motion becomes

$$\gamma_0 \frac{\partial^2 \vec{r}}{\partial t^2} = \frac{\partial}{\partial s}\left(T\hat{t}\right) + \vec{f}\,, \tag{1}$$

$$\hat{t} = \frac{\partial \vec{r}}{\partial s}\left|\frac{\partial \vec{r}}{\partial s}\right|^{-1}\,, \tag{2}$$

where γ_0 is the cable mass per unit length, T is the cable tension force magnitude, $\hat{t}$ is the tangential

unit vector of the cable. The variable f represents all external forces made up of (i) added mass and Froude-Krylov forces, (ii) net force of gravity and buoyancy, (iii) contact forces, typically from sea-floor interaction and (iv) drag forces (see [25] for details).

E. Floater dynamics

Floaters and sinkers are common mooring components in offshore engineering. They are used to introduce a hydrodynamic spring stiffness to the mooring system. As such they are commonly designed to be submerged at all times to avoid the structural forces in the splash zone, and they are typically small in relation to changes in the fluid velocity due to wave motion or ocean currents.

The equation of motion of a submerged rigid body (floater/sinker) connected to N cables reads

$$\frac{\mathrm{d}}{\mathrm{d}t}\left(\mathbf{M}^f\vec{u}\right) = \vec{F}_{\mathrm{a}}^f + \vec{F}_{\mathrm{b}}^f + \vec{F}_{\mathrm{d}}^f + \sum_{i=0}^{N}\vec{F}_i\,, \tag{3}$$

where $\mathbf{M}^f$ is the 6x6 mass matrix, $\vec{u}^{\mathrm{T}} = \left[\vec{v}^{\mathrm{T}}\,\vec{\omega}^{\mathrm{T}}\right]$ is the 6-degrees of freedom velocity vector representing linear ($\vec{v}$) and rotational $\vec{\omega}$ velocity. Further, $\vec{F}_{\mathrm{a}}^f$ are the added mass forces, $\vec{F}_{\mathrm{b}}^f$ are the buoyancy forces and $\vec{F}_{\mathrm{d}}^f$ are the drag forces. We now introduce the body-fixed Lagrangian coordinate system $\mathcal{I} = \left(\hat{\imath},\hat{\jmath},\hat{k}\right)$, and let $\vec{b} = [b_0\,b_1\,b_2\,b_3]$ be the quaternion relating $\mathcal{I}$ to the inertial frame ($\mathcal{X}$) orientation. Then the rotation matrix $\mathbf{R}$ is the transform of vector components from $\mathcal{X}$ to $\mathcal{I}$, and it is expressed from $\vec{b}$ as

$$\mathbf{R} = \begin{bmatrix} \sigma_b + B_{11} & B_{12} + B_{03} & B_{13} - B_{02} \\ B_{21} - B_{03} & \sigma_b + B_{22} & B_{23} + B_{01} \\ B_{31} + B_{02} & B_{32} - B_{01} & \sigma_b + B_{33} \end{bmatrix}. \tag{4}$$

in which $B = 2\left(\vec{b}\otimes\vec{b}\right)$, and $\sigma_b = b_0^2 - b_1^2 - b_2^2 - b_3^2$.

The position of the center of gravity $\vec{O}_{\mathcal{X}}$ and the quaternion of rotations b are updated from the linear velocity $\vec{v}$ and the angular velocity $\vec{\omega}$ as

$$\frac{\partial\vec{O}_{\mathcal{X}}}{\partial t} = \mathbf{R}^{\mathrm{T}}\vec{v}\,, \tag{5}$$

$$\frac{\partial\vec{b}}{\partial t} = \frac{1}{2}\begin{bmatrix} b_0 & -b_1 & -b_2 & -b_3 \\ b_1 & b_0 & -b_3 & b_2 \\ b_2 & b_3 & b_0 & -b_1 \\ b_3 & -b_2 & b_1 & b_0 \end{bmatrix}\begin{bmatrix} 0 \\ \vec{\omega} \end{bmatrix}. \tag{6}$$

Please note that $\vec{O}_{\mathcal{X}}$ is the position expressed in the inertial frame $\mathcal{X}$, while all other state vectors are in the $\mathcal{I}$ frame of reference. Expressing (3) in $\mathcal{I}$ and separating the translational and rotational modes of motion results in

$$\begin{bmatrix} m\dfrac{\partial\vec{v}}{\partial t} \\ \mathbf{I}\dfrac{\partial\vec{\omega}}{\partial t} \end{bmatrix} = -\begin{bmatrix} \vec{\omega}\times m\vec{v} \\ \vec{\omega}\times\mathbf{I}\vec{\omega} \end{bmatrix} + \vec{F}_{\mathrm{a}}^f + \vec{F}_{\mathrm{b}}^f + \vec{F}_{\mathrm{d}}^f + \sum_{i=0}^{N}\vec{F}_i\,, \tag{7}$$

$$\vec{F}_{\mathrm{b}}^f = \begin{bmatrix} \left(m - V\rho_{\mathrm{f}}\right)\mathbf{R}\vec{g} \\ -\vec{OB}\times V\rho_{\mathrm{f}}\mathbf{R}\vec{g} \end{bmatrix}, \tag{8}$$

$$\vec{F}_i = \begin{bmatrix} \mathbf{R}\vec{T}_i \\ \vec{OM}_i\times\mathbf{R}\vec{T}_i + \mathbf{R}\vec{M}_i \end{bmatrix}, \tag{9}$$

where m is the floater mass, $\mathbf{I}$ is the inertia matrix of the floater (3x3), V is the volume of the floater and $\vec{OB}$ and $\vec{OM}_i$ are the vectors from the centre of mass to the centre of buoyancy and to the attachment point of mooring cable i respectively. The expressions for added mass and drag damping are a bit more complicated. The following expressions are derived for a cylindrical floater, with Lagrangian frame $\mathcal{I}$ located in the geometrical center and $\hat{k}$ along the symmetry axis. Assuming that the size of the body is small in comparison with changes in the surrounding flow field, we set $\vec{v}_{\mathrm{f}} = \vec{v}_{\mathrm{O}}$ and $\partial\vec{v}_{\mathrm{f}}/\partial t = \vec{a}_{\mathrm{O}}$ to be constant over the entire body domain, evaluated at the origin of $\mathcal{I}$. Then for added mass $\vec{F}_{\mathrm{a}}^f$, we can compute the forces as

$$\vec{F}_{\mathrm{a}}^f = V\rho_{\mathrm{f}}\begin{bmatrix} \vec{a}_{\mathrm{O}\perp}\left(1 + C_{\mathrm{M1}}\right) - C_{\mathrm{M1}}\dot{\vec{v}}_{\perp} \\ \left(1 + \dfrac{2}{h}C_{\mathrm{M2}}\right)a_{\mathrm{O}\hat{k}} - \dfrac{2}{h}C_{\mathrm{M2}}\dot{v}_{\hat{k}} \\ -\dfrac{h^2}{12}C_{\mathrm{M1}}\dot{\vec{\omega}}_{\perp} \\ 0 \end{bmatrix}. \tag{10}$$

Here the index $\perp$ denotes vector projection onto the $\hat{\imath},\hat{\jmath}$ plane and h is the cylinder height. Coefficients C_{M1} and C_{M2} are the in-plane and out of plane added mass coefficients of a circle respectively. The factor $h^2/12$ comes from pre-integrating the moment equation for each cross-section along the cylinder. In the case of drag forces however, their quadratic nature makes the pre-integrated expressions exceedingly complex and a simple quadrature routine will perform equally well. So, we leave the expression in integral form as

$$\vec{F}_{\mathrm{d}}^f = \frac{\rho_{\mathrm{f}}}{2}\begin{bmatrix} C_{\mathrm{D1}}D\int_{-h/2}^{h/2}\sqrt{\vec{v}_{\perp}^*\cdot\vec{v}_{\perp}^*}\,\vec{v}_{\perp}^*\,\mathrm{d}r \\ \left(C_{\mathrm{D2}}\frac{\pi D^2}{4} + C_{\mathrm{D3}}Dh\right)\left|v_{\hat{k}}^*\right|v_{\hat{k}}^* \\ C_{\mathrm{D1}}D\int_{-h/2}^{h/2} r\sqrt{\vec{v}_{\perp}^*\cdot\vec{v}_{\perp}^*}\left(\hat{k}\times\vec{v}_{\perp}^*\right)\mathrm{d}r \\ C_{\mathrm{D3}}Dh\frac{D^2}{4}\left|\omega_{\hat{k}}\right|\omega_{\hat{k}} \end{bmatrix}, \tag{11}$$

where C_{D1}, and C_{D2} are the in-plane and out of plane drag coefficients of a circle respectively, and C_{D3} is the shear coefficient of tangential drag. D is the cylinder diameter and $\vec{v}^* = \vec{v}_{\mathrm{O}} - \vec{v} - \vec{\omega}\times r\hat{k}$.

III. Numerical model

The numerical model used in this paper is the high-order discontinuous Galerkin (DG) model, denoted Moody. For completeness the numerical techniques are briefly outlined below, for details see [25], [26], [28]. Moody has been coupled to the CFD code OpenFOAM [29], [30] and to the linear code WEC-Sim [31], [32], enabling coupled mooring dynamics via the motion and the tension force at the fair-lead point of the mooring. In this study, however, Moody will be run as stand-alone module using circular motion of the fair-lead point with varying amplitude a_w and period time T_w.

F. Discontinuous Galerkin method

Moody solves (1) using an hp-adaptive discontinuous Galerkin (DG) method, where h denotes the

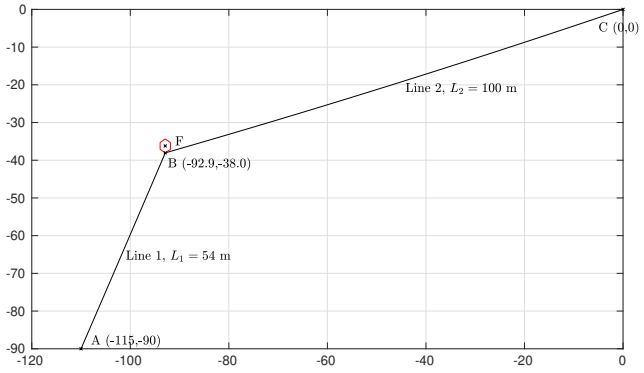

Fig. 2. Layout of the mooring system at equilibrium, showing the location of points *A*, *B*, *C* and *F* in the mooring leg.

mesh size and p the polynomial order within each element. The hallmark of the DG methods is that the solutions are discontinuous across element boundaries and the elements are coupled together by numerical fluxes as in the finite volume method. This makes the DG method locally conservative and a good candidate for problems involving shocks, such as snap loads. In Moody the basis functions are made up of Legendre polynomials and the local Lax-Friedrich flux is used as numerical flux. For smooth solutions, Moody exhibits convergence rates of $(p + 1/2)$ [25]. This allows high-resolution solutions using few degrees-of-freedom. Solutions of shock waves can be made monotone by locally lowering the polynomial order to linear and apply standard slope limiters. In this work, we focus on snap load identification rather than quantification, which is why a constant $p = 4$ mesh order was used throughout the simulation campaign. The model advances in time using the explicit third-order strong-stability-preserving Runge-Kutta scheme.

G. Floater and sinker discretization

The discontinuous nature of the finite element space makes the coupling to submerged rigid bodies easily achieved. All cable ends connected to a rigid body are treated as Dirichlet boundary conditions, where the boundary condition values of velocity are taken from the point velocity of the rigid body. At the same time, the rigid body dynamics model collect the tension forces and moments from all connected cables, and use them to compute the effective total force and moment.

The equations of motion for the floater have been presented in Section II-E. The state vector of the rigid floater/sinker is described by 13 degrees of freedom,

$$\vec{U}^{f^{\mathrm{T}}} = \left[\vec{O}_{\mathcal{X}}^{T}, \vec{b}^{T}, \vec{u}^{T}\right]^{\mathrm{T}}, \tag{12}$$

where $\vec{O}_{\mathcal{X}}$ is the floater position (centre of gravity) in the inertial frame and the other vectors are in the Lagrangian body frame $\mathcal{I}$. In the implementation of (3) we assume that the body is submerged at all times, which enables a constant and diagonal mass matrix describing inertial effects of the body and the surrounding fluid as

TABLE I
CHARACTERISTICS OF THE POLYESTER ROPE USED IN THE SIMULATIONS.

Symbol	Unit	Value	Description
γ_0	kg/m	4.9	Mass per meter
ρ_{c}	kg/m^3	1362	Material density
d_{c}	m	0.08	Diameter for drag force
C_{Mn}	-	1.0	Added mass coefficient
C_{Dt}	-	0.1	Tangential drag coeff.
C_{Dn}	-	1.0	Normal drag coeff.
$T(\epsilon)$	N	$\sum_{i=1}^{i=5} C_{\epsilon}^{(i)} \epsilon^i$	Strain-force relation[a]

[a] The coefficients of the strain-force relation are $C_{\epsilon}^{(i)} = [5.8238, 66.701, 1006.6, 1294.2, 13367]$ MN, for $i = 1$ to $i = 5$ respectively.

$$\mathrm{diag}\left(\mathbf{M}_{\mathrm{e}}^{f}\right) = \begin{bmatrix} m + V\rho_{\mathrm{f}} C_{\mathrm{M1}} \\ m + V\rho_{\mathrm{f}} C_{\mathrm{M1}} \\ m + \dfrac{2V\rho_{\mathrm{f}} C_{\mathrm{M2}}}{h} \\ I_{\hat{i}} + \alpha_h C_{\mathrm{M1}} \\ I_{\hat{j}} + \alpha_h C_{\mathrm{M1}} \\ I_{\hat{k}} \end{bmatrix}, \tag{13}$$

with $\alpha_h = h^2/12$, derived from (10). The constant inverse of $\mathbf{M}_e^f$ is then trivially computed. The integrals in (11) are integrated using a 7 point Gauss-Lobatto-Legendre quadrature, see e.g. [33], on a 5^{th} order Legendre polynomial. Forces and moments from each mooring cable are computed in $\mathcal{I}$ based on the attachment point location $O\vec{M}_i$, see (9). The position and velocity of point $\vec{M}_i$ in $\mathcal{X}$ are then

$$\vec{M}_i^{(\mathcal{X})} = \vec{O}_{\mathcal{X}} + R^{\mathrm{T}} O\vec{M}_i\,, \tag{14}$$

$$\frac{\partial \vec{M}_i^{(\mathcal{X})}}{\partial t} = R^{\mathrm{T}}\left(\vec{v} + \vec{\omega} \times O\vec{M}_i\right), \tag{15}$$

which are used as boundary conditions for any cable connected to attachment point M_i.

IV. TEST CASE

We consider the typical setup of a mooring system using polyester rope mooring lines in a moderate water depth of 90 m. The mooring leg consists of one floater and two ropes of polyester type (see Table III-G for material data). As is depicted in Fig. 2, Line 1 (L_1) extends from the anchor point *A* to the floater connection point *B*, and Line 2 (L_2) connects point *B* to the fair-lead point *C*. Point *F* represents the centre of gravity (cog) of the floater. The mooring force at point *A* is taken from the end-point ($s = 0$) of Line 1, and the force at point *B* is sampled at $s = 0$ of Line 2, i.e. in the top mooring line. The force at point *C* is sampled at $s = L$ of Line 2, being the fair-lead position.

To highlight the importance of the dynamic effects of the floater on the resulting mooring tension, we will look at the mooring response using periods $T_{\mathrm{w}} \in [1, 10]$ s and amplitudes $a_w = 0.5$ m and $a_w = 1$ m, representing a prescribed sinusoidal fair-lead motion. The lines L_1 and L_2 were discretised in Moody using 5 and 10 elements respectively. A polynomial order 4 was used and a CFL-condition of 0.9 was applied to control time step size.

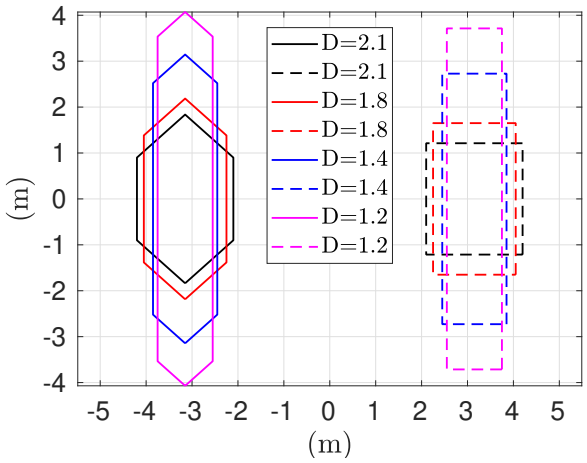

Fig. 3. Two-dimensional view of the floater dimensions. Solid lines are actual cross section, dashed lines represent equivalent cylinder. See Table II for details.

H. Floater characteristics

The baseline floater design is the one used in the work of Yang and co-workers [20], [34], [35]. The floater geometry was in those studies in the generic form of a cylinder with a diameter of 2.1 m with cones mounted on each lid. Based on that geometry a series of four cylindrical floaters are generated. The cylinders have varying slenderness but constant volume. Fig. 3 illustrates the different geometries investigated in this study while the data for the floaters are found in table II. We will refer to the cylinder with $D = 2.1\,\mathrm{m}$ as the baseline floater (D_0). The different floater geometries are for each floater computed from the diameter, D, and the constant volume V_0 as

$$h_{\mathrm{tot}} = \frac{V_0 - 2V_{\mathrm{c}}}{0.25\pi D^2} + 2kD\,, \tag{16}$$

$$h_{\mathrm{eff}} = \frac{V_0}{0.25\pi D^2}\,, \tag{17}$$

$$V_{\mathrm{c}} = 0.25\pi D^2 kD\,, \tag{18}$$

$$z_{\mathrm{B}} = -0.5h_{\mathrm{tot}}\,, \tag{19}$$

where h_{tot} is the height of the floater with the cones, h_{eff} is the height of the equivalent cylinder, z_{B} is the coordinate of the mooring attachment to the cylinder, V_{c} is the volume of the cone and $k = (0.937/2.1)$ is the cone slope, which is also assumed constant over the different floater diameters. Please note that the mooring attachment of the baseline test is $z_{\mathrm{B}} = -1.837\,\mathrm{m}$ compared with the original value of $z_{\mathrm{B}} = -1.8\,\mathrm{m}$ presented in [34]. This is a consequence of the conical lid assumption. From the perspective of this generic study, the difference is acceptable. Further, note that the cog (point *F*) will be translated in the vertical direction at the initial position, but due to the preserved buoyancy the moorings and point *B* will remain at the same initial equilibrium location as shown in Fig. 2 for all floater variations.

V. Results

The results are divided into two parts. First we analyse the physical dependence on floater dynamics.

TABLE II
Data for the four floater geometries. D_0 denotes the baseline floater.

Symbol	D_0	D_1	D_2	D_3
D (m)	2.1	1.8	1.4	1.2
h_{eff} (m)	2.5696	3.4975	5.7815	10.2783
z_{B} (m)	-1.8373	-2.2842	-3.3072	-5.4515
I_{xx} (kgm^2)	2220.7	3220.58	7551.1	13592
I_{zz} (kgm^2)	1598.6	1174.5	710.5	522.0

We then continue with the difference between floater designs in a second part.

I. Baseline floater

Fig. 4 shows the results of a (amplitude, period)= $(a_w, T_w) = (1\mathrm{m}, 5\mathrm{s})$ test case for the last 20 s of simulation. This represents the idealised motion of the fair-lead given by a regular wave with wavelength (λ) 40 m of 5% steepness ($2a/\lambda$). From Fig. 4 (a) and (c) we note some features of the dynamic mooring response:

- The minimum tension goes to zero in L_2, which indicates risk of slack-snap behaviour. On the other hand, the snap loads generated by the re-entry into the taught regime are very small. This can be deduced from the minor differences between point *B* and *C* forces in Fig. 4a. The tension force is in this case more or less homogeneous along the cable. Therefore the mooring forces at the fair-lead are still clearly dominated by the first order frequency response.
- The lower cable is (as expected) always under tension. However, its force response has a much stronger coupling to the floater motion shown in Fig. 4c, with a clear higher frequency response.
- Point *F* on the floater only shows first order response. The excitation of the pendulum system of the floater (suspended from point *B*) clearly also triggers an overtone in pitch response, which primarily affects the horizontal motion of point *B*. However, due to the geometric constraints of the mooring, the connection with L_2 also triggers a vertical oscillation in the higher frequency.

Looking at a more severe case of ($a_w = 1\mathrm{m}, T_w = 4\mathrm{s}$), which represents the idealised response of a wave with 8 % steepness, the tension force of L_1 goes into a bi-harmonic state where the second harmonic is extremely clear in the response. Now, also the snap loads on L_2 are more clearly seen, where the return frequency of the snap load is observed in the high-frequency peaks at point *B* and *C*. This claim is further supported by observing the time offset between the red and the blue curves of Fig. 4b. Worth to note is that although the higher-order content of the floater motion is clearly higher in Fig. 4d than in Fig. 4c, the surge motion of the center of gravity is still fairly smooth due to its large inertial properties.

In Figs. 5a and 5b we consider the response over a wider range of frequencies. The amplitude is here smaller with $a_w = 0.5$ m excitation, and we can

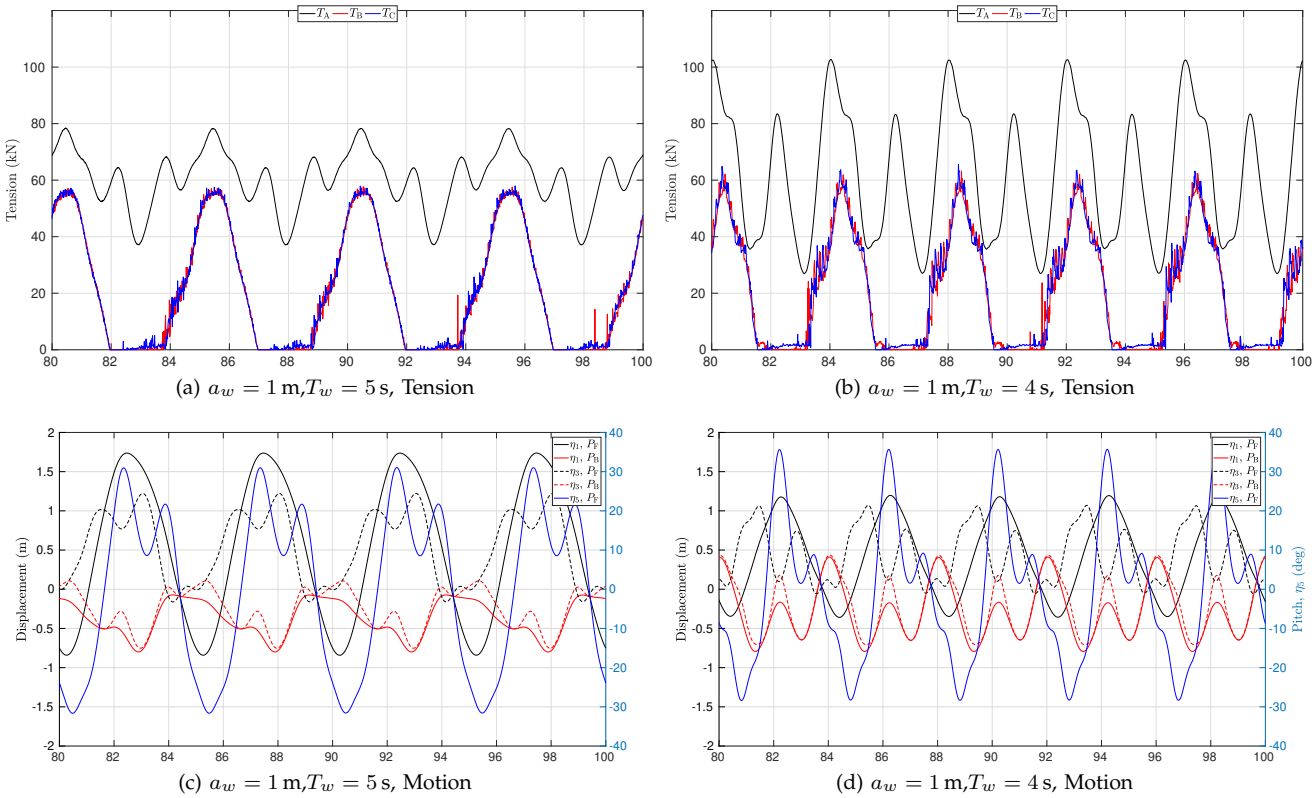

(a) $a_w = 1\,\text{m}, T_w = 5\,\text{s}$, Tension
(b) $a_w = 1\,\text{m}, T_w = 4\,\text{s}$, Tension
(c) $a_w = 1\,\text{m}, T_w = 5\,\text{s}$, Motion
(d) $a_w = 1\,\text{m}, T_w = 4\,\text{s}$, Motion

Fig. 4. Mooring response for test case $a_w = 1\,\text{m}$ at $T_w = 5\,\text{s}$ (a),(c) and $T_w = 4\,\text{s}$ (b),(d) respectively. (a),(b) Tension at points *A*, *B* and *C* (see Fig. 2). (c),(d): Displacements of points *B* and *F*, including floater pitch angle

more clearly see the connection between frequencies amplifying the dynamic tension (represented by the minimum, T^-, and maximum T^+ tension) and the motion response of the floater.

J. Impact of floater design

Results from the four different floaters geometries are presented in Fig. 5 for excitation amplitude $a_w = 0.5\,\text{m}$. All floaters exhibit a region of resonance where the floater surge motion is more amplified. The main differences in floater design are related to that for a decreasing diameter, both the moment of inertia I_{xx} and the distance z_B from floater centre to attachment point *B* increase, see Table II. This is confirmed by the decreasing pitch response with increasing floater diameter, see Fig. 5. The largest difference in system response is changing from D_1 to D_2 where the slack region is avoided completely for D_2 and D_3, hence more effectively avoiding many of the dangers of slack-snapping mooring response.

In the baseline (D_0) case, depicted in Fig. 5b, the surge peak is at $T_w = 6\,\text{s}$ with a value three times higher than the excitation amplitude. However, the maximum tension force in Line 2 is in Fig. 5a found at $T_w = 5.5\,\text{s}$. This trend is evident throughout the floater diameters. The surge amplitude of the floater peaks at a lower frequency than the force response in Line 2. Instead, the trends in the motion spectrum of floater pitch response matches very well with the fairlead tension force (at point C) for all floater designs studied, especially regarding the resonance peak.

The results presented in Fig. 5 also show that the response in Line 1 is more clearly coupled to the floater motion, albeit it does not become slack in any scenario tested here. The maximum force at the anchor T_A^+ has additional peaks at $T_w = 4\,\text{s}$, and at $T_w = 2\,\text{s}$. These peaks can also be found in the motion spectra of heave and pitch in the right column of Fig. 5. With increasing floater diameter, the peaks are abated and are of minor importance for the behaviour in D_2 and D_3.

Fig. 6 provides a deeper insight into the floater geometry difference at $T_w = 4\,\text{s}$ and compares the forces and floater response at amplitudes $a_w = 0.5\,\text{m}$ and $a_w = 1\,\text{m}$ for the $T_w = 4\,\text{s}$ load case. There are substantial differences. First, the peak force amplitudes are substantially higher in D_0 compared with D_2. In Line 2, this is attributed to the slack-snap behaviour seen in D_0 but avoided in D_2. In Line 1 however, we can clearly see a much larger second harmonic response in D_0 than in D_2, which is connected to the difference in the rotational mode response of the floaters. This is further supported by the differences in motion of point *B* in Figs. 6b and 6d.

VI. Discussion

The results have shown a distinct connection between mooring force response and the dynamic properties of the floater. Consequently, the results are sensitive to the magnitudes of the inertia, added mass and the viscous damping properties of the floaters. We used values from the literature for the sectional drag and added mass coefficients, and neglected end-point effects in the calculation of the global floater coefficient.

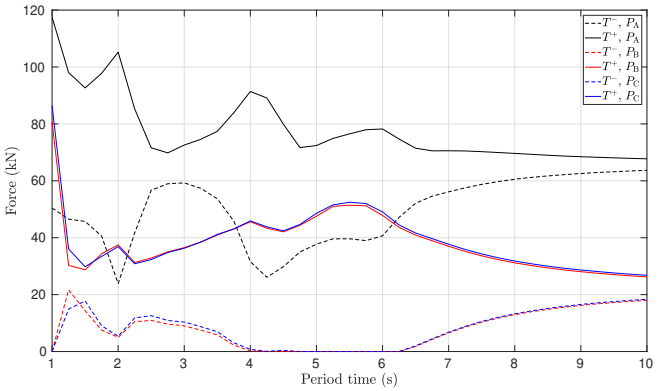

(a) Force, D_0

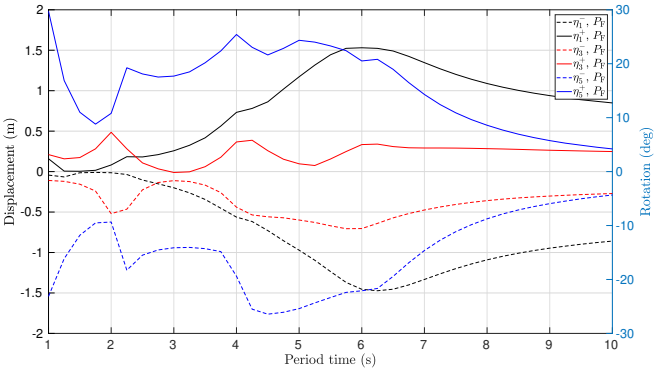

(b) Motion, D_0

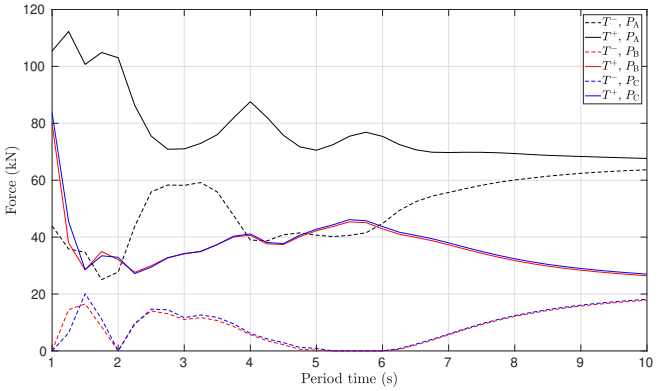

(c) Force, D_1

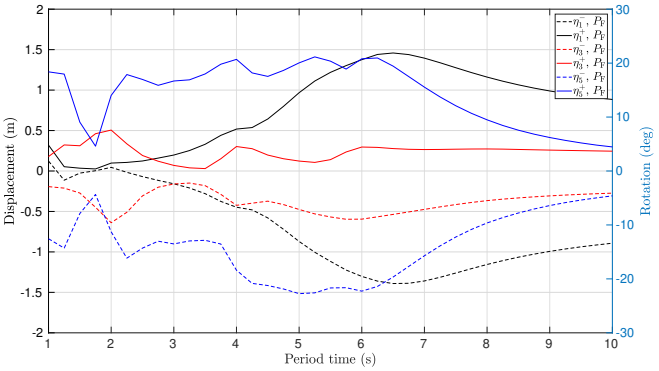

(d) Motion, D_1

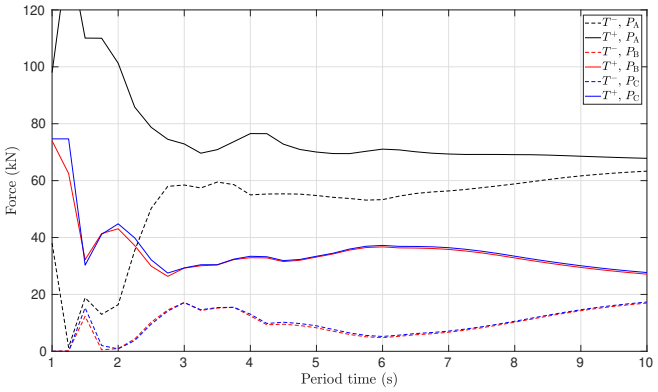

(e) Force, D_2

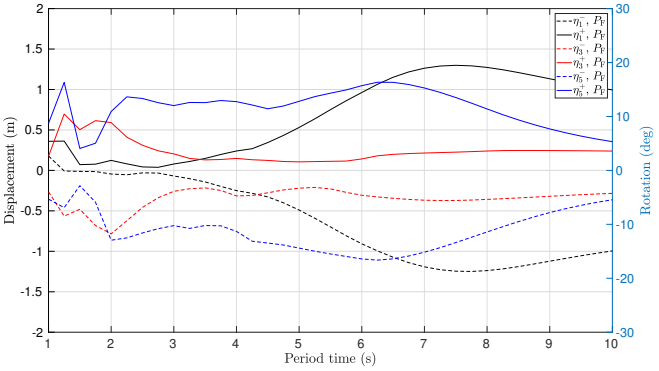

(f) Motion, D_2

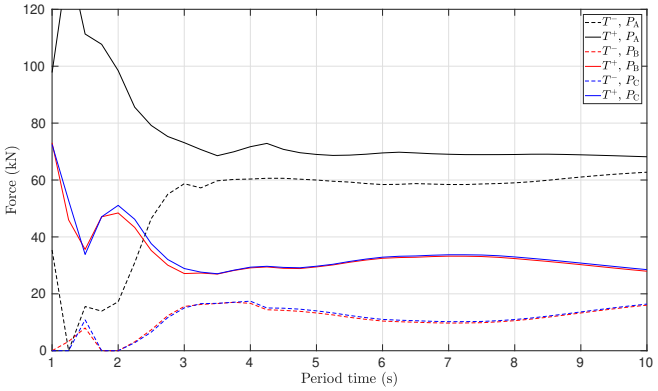

(g) Force, D_3

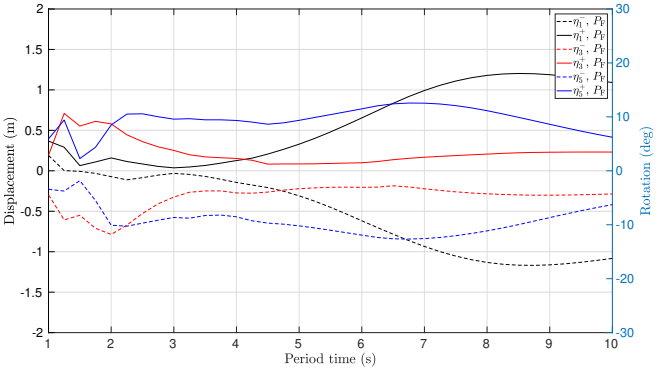

(h) Motion, D_3

Fig. 5. Maximum and minimum response of the different floater configurations (top to bottom : D_0, D_1, D_2, D_3) for $a_w = 0.5\,\mathrm{m}$ at different period times. Left side (i.e. (a), (c), (e), (g)) shows tension forces at points A, B and C, see Fig. 2. Right side shows floater motion in surge (η_1), heave (η_3) and pitch (η_5).

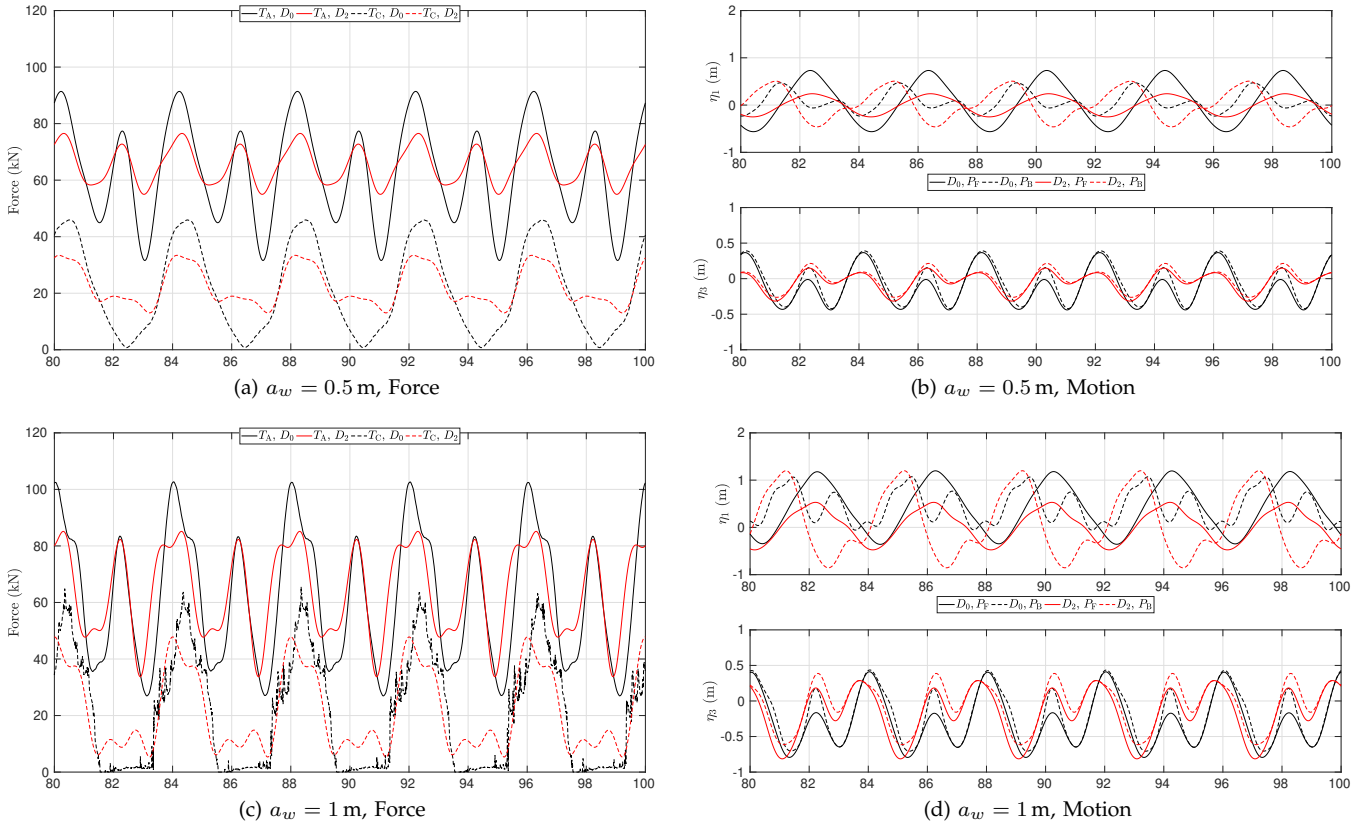

(a) $a_w = 0.5$ m, Force (b) $a_w = 0.5$ m, Motion

(c) $a_w = 1$ m, Force (d) $a_w = 1$ m, Motion

Fig. 6. (a), (c) Time series of mooring forces at points A (anchor), and C (fair-lead). (b), (d) Motion over time of the floater centre of gravity (point F) and the mooring attachment point B. Comparison between response from floater D_0 and D_2 for $T_w = 4$ s at two different excitation amplitudes: $a_w = 0.5$ m (a),(b), and $a_w = 1$ m (c),(d)

Also, the moment of inertia of the stretched floaters was calculated from the baseline value under the assumption of a uniform density. Arguably we have some uncertainty in the absolute values of the results, and the actual thresholds of slack/snap behaviour or maximum forces should therefore be viewed as indicative. A more elaborate sensitivity analysis of the system parameters is judged to be out of scope of this paper. Although this is a limitation of the current work, the results show coherent trends between floater rotation and mooring response that are important to understand when designing mooring legs with floaters. We further argue that the proposed method is a step towards a more complete analysis, as the rotational dynamics the floater are either neglected [18] or linearised [17], [27] in well-adopted approaches.

VII. Conclusion

We have presented a numerical study on the importance of floater dynamics for mooring system response. We have provided an extensive analysis of a common mooring leg consisting of two lines and an intermediate floater, with varying floater geometry (keeping the net buoyancy constant). Tension forces and floater displacement have been presented based on circular excitation of the fair-lead point.

Under the assumptions of the method and with some uncertainty in the hydrodynamic coefficients of the floaters, the results show that the dynamic properties of the floater can have a substantial impact on the mooring design, in particular when it comes to avoiding slack-snap behaviour. For the cases shown in this paper, a floater with a higher moment of inertia is preferable over one with a more high-frequent pitch response. Therefore, making the baseline cylindrical floater of $D = 2.1$ m diameter longer and thinner, significantly reduced the region of slack for the upper cable (Line 2), see Fig. 6. For an excitation amplitude of $a_w = 0.5$ m, the $D_2 = 1.4$ m diameter floater was enough to avoid any slack in the system over the frequencies studied, see Fig. 5. The mooring force response resonance period coincides with the maximum pitch response, and occurs at a higher frequency than the maximum surge amplification of the floater. Further studies using experimental data or CFD analysis to quantify the hydrodynamic properties of the floaters in greater detail would be very beneficial for the continued development of this topic. This would also enable a validation suite for numerical tools simulating this type of mooring leg, designed for large amplitude motion.

We recommend that more studies focusing on the intricate dynamic interaction between floater and mooring cables are made, and emphasize that the rotational modes of motion should be considered in optimal floater selection, where traditionally only net buoyancy and mass have been taken into account.

Acknowledgement

The authors want to thank Dr. Shun Han Yang at Chalmers University of Technology for providing the

information about the baseline mooring design.

REFERENCES

[1] J. Fitzgerald, "Position mooring of wave energy converters," Ph.D. dissertation, Chalmers University of Technology, 2009.

[2] *Waves 4 Power Homepage*, Waves 4 Power AB, 2019.

[3] P. Vicente, A. Falcao, L. Gato, and P. Justino, "Dynamics of arrays of floating point-absorber wave energy converters with inter-body and bottom slack-mooring connections," *Ocean Engineering*, vol. 31, pp. 267–281, 2009.

[4] P. Ricci, A. Rico, P. Ruiz-Minguela, F. Boscolo, and J. Villate, "Design, modelling and analysis of an integrated mooring system for wave energy arrays," in *Proc. 4th International Conference on Ocean Energy*, Dublin, Ireland, 2012.

[5] OES, "Ocean Energy Systems: Annual report 2016." 2016.

[6] *Position Mooring*, Det Norske Veritas, 2010, offshore standard DNV-OS-301.

[7] M. Dhanak and X. Nikolaos, *Handbook on Ocean Engineering*. Springer verlag, 2016.

[8] C. Hennessey, N. Pearson, and R. Plaut, "Experimental snap loading of synthetic ropes," *Shock and Vibration*, vol. 12, pp. 163–175, 2005.

[9] M. Triantafyllou, A. Bliek, and H. Shin, "Dynamic analysis as a tool for open-sea mooring system design." *SNAME Transactions*, vol. 93, pp. 302–324, 1985.

[10] J. Gobat and M. Grosenbaugh, "Dynamics in the trouchdown region of catenary moorings," in *Proc. 11th International Offshore and Polar Engineering Conference*, Stavanger, Norway, 2001.

[11] A. Tjavaras, "The dynamics of highly extensible cables," Ph.D. dissertation, Massachusetts Institute of Technology, 1996.

[12] P. Thies, L. Johanning, and G. Smith, "Lifecycle fatigue load spectrum estimation for mooring lines of a floating marine energy converter," in *Proc. 31st International Conference on Ocean, Offshore and Arctic Engineering*, Rio de Janeiro, Brazil, July 2012.

[13] A. Savin, O. Svensson, and M. Leijon, "Azimuth-inclination angles and snatch load on a tight mooring system," *Ocean Engineering*, vol. 40, pp. 40–49, 2012.

[14] M. Hann, D. Greaves, and A. Raby, "Snatch loading of a single taut moored floating wave energy converter due to focussed wave groups," *Ocean Engineering*, vol. 96, pp. 258–271, 2015.

[15] V. Harnois, "Analysis of highly dynamic mooring systems: Peak mooring loads in realistic sea conditions," Ph.D. dissertation, University of Exeter, 2014.

[16] J. Morison, M. O'Brien, J. Johnson, and S. Schaaf, "The force exerted by surface waves on piles," *Petroleum Transactions, Amer. Inst. Mining Engineers*, vol. 186, pp. 149–154, 1950.

[17] S. Mavrakos, V. Papazoglou, M. Triantafyllou, and J. Hatjigeorgiou, "Deep water mooring dynamics," *Marine Structures*, vol. 9, pp. 181–209, 1996.

[18] J. Yan, D. Qiao, and J. Ou, "Optimal design and hydrodynamic response analysis of deep water mooring system with submerged buoys," *Ships and Offshore Structures*, vol. 13, no. 5, pp. 476–487, 2018.

[19] D. Pizer, C. Retzler, R. Henderson, F. Cowieson, M. Shaw, B. Dickens, and R. Hart, "Pelamis WEC - recent advances in the numerical and experimental modelling programme," in *Proceedings of the 6th European Wave and Tidal Energy Conference*. Glasgow, UK: The International Society of Offshore and Polar Engineers (ISOPE), August 2005.

[20] X. Lang, S.-H. Yang, J. Ringsberg, E. Johnson, C. G. Soares, and M. Rahm, "Comparison between full-scale measurements and numerical simulations of mooring forces in a floating point-absorbing WEC system," in *Advances in Renewable Energies Offshore - Proceedings of The 3rd International Conference on Renewable Energies Offshore*. Lisbon, Portugal: Taylor and Francis Group, October 2018, pp. 865–873.

[21] J. Fitzgerald and L. Bergdahl, "Considering mooring cables for offshore wave energy converters," in *Proc. 7th European Wave and Tidal Energy Conference*, Oporto, Portugal, 2007.

[22] G. Paredes, J. Palm, C. Eskilsson, L. Bergdahl, and F. Taveira-Pinto, "Experimental investigation of mooring configurations for wave energy converters," *Int. J. of Marine Energy*, vol. 15, pp. 56–67, 2016.

[23] P. Vicente, A. Falco, and P. Justino, "Optimization of mooring configuration parameters of floating wave energy converters," in *Proceedings of the ASME 2011 30th International Conference on Ocean, Offshore and Arctic Engineering*, Rotterdam, the Netherlands, June 2011, pp. 759–765.

[24] J. Ortiz, H. Bailey, B. Buckham, and C. Crawford, "Surrogate based design of a mooring system for a self-reacting point absorber," in *Proc. 25th International Offshore and Polar Engineering Conference*, Kona,Hawaii, 2015.

[25] J. Palm, C. Eskilsson, and L. Bergdahl, "An hp-adaptive discontinuous Galerkin method for modelling snap loads in mooring cables," *Ocean Engineering*, vol. 144, pp. 266–276, 2017.

[26] J. Palm, "Mooring Dynamics for Wave Energy Applications," Ph.D. dissertation, Chalmers University of Technology, 2017.

[27] *OrcaFlex manual – version 9.5a*, Orcina Inc, 2012.

[28] J. Palm and C. Eskilsson, *MOODY, User's manual version 1.0*, 2018, avaliable www.github.com/johannep/moodyAPI/releases.

[29] *OpenFOAM Homepage*, OpenCFD Ltd, 2018, available http://www.openfoam.org.

[30] J. Palm, C. Eskilsson, G. Paredes, and L. Bergdahl, "Coupled mooring analysis for floating wave energy converters using CFD: Formulation and validation," *Int. J. of Marine Energy*, vol. 16, pp. 83–99, 2016.

[31] *WEC-SIM Homepage*, NREL and Sandia Corp., 2015, available http://wec-sim.github.io/WEC-Sim.

[32] G. M. Paredes, C. Eskilsson, J. Palm, J. P. Kofoed, and L. Bergdahl, "Coupled BEM/*hp*-FEM modelling of moored floaters," in *Proceedings of the 1st Vietnam Symposium on Advances in Offshore Engineering*. Hanoi, Vietnam: Springer, November 2018, pp. 504–510.

[33] G. E. Karniadakis and S. Sherwin, *Spectral/hp Element Methods for CFD*, 2nd ed. New York, Oxford: Oxford University Press, 2003.

[34] S.-H. Yang, "Analysis of the fatigue characteristics of mooring lines and power cables for floating wave energy converters," Ph.D. dissertation, Chalmers University of Technology, 2018.

[35] S. Yang, J. Ringsberg, E. Johnson, Z. Hu, and J. Palm, "A comparison of coupled and de-coupled simulation procedures for the fatigue analysis of wave energy converter mooring lines," *Ocean Engineering*, vol. 117, pp. 332–345, 2016.